Characterization of the Electromagnetic Response of GPR Systems Using Boundary Integral Equations and Boundary Elements Methods

Pedro Ramaciotti Morales
12th December 2009

***Abstract*—Ground penetrating radar has arisen as a prominent technology for landmine detection but whereas several studies treat the subject of appropriate radar design and remote sensing techniques, few deal with the particular electromagnetic response of the mines to be detected, which can vary significantly in the gamut of existing landmines. With the purpose of analyzing such response a method based on experimental data and BEM techniques applied to the boundary integral equation is developed to solve the scattered radar wavefronts. The electromagnetic response over a frequency range and the angular dispersion pattern of an anti-personnel and an anti-tank mine is studied.**

***Index Terms*—Ground penetrating radar, radar cross section, radar remote sensing, boundary integral equation, boundary elements method, humanitarian demining.**

I. Introduction

DESPITE decades of scientific effort landmine detection and removal capabilities remain unable to meet society's demining's needs. As of 2010, antipersonnel landmines were still laid in over 66 countries, and a total 3,956 new casualties were recorded during 2009, while many more are estimated to go unrecorded [1], [2]. Together with human losses landmines cause a great deal of economical damage in terms of treatment of victims and the incapability of using mined terrain.

The removal of landmines is the ultimate goal of the global humanitarian demining effort, however, the existing techniques put this goal far in the future due to time constraints, costs, reliability requirements and safety issues. In the recent past decades the technological effort has been focused on creating and using technology for detecting underground mines permitting properly isolation of hazardous areas and accurate location of mines for future removal. Among the techniques used for detection the magnetic induction and GPR imaging are the most common. The detection by magnetic induction has reached the culmination of 70 years of development with notable progresses, but depends on the amount of metal present in the mines for detection. For this reason, modern mines are constructed with negligible amounts of metal (Minimum Metal Mines), using plastic cases and mechanisms, with many reaching as little metal content as 1 gram (e.g., the Belgian PRB-M409 or the Italian VS-50 landmines, [3]). In this modern setting the difficulty of detection by induction is dealt primarily by the addition of techniques for imaging the subsurface using ground penetrating radars (GPR), which can observe slight inhomogeneities such as plastic mines underground. A complete historical review can be found in [4] and [5].

Pedro Ramaciotti is with Escuela de Ingeniería, Pontificia Universidad Católica de Chile.

The GPR detection capability depends on the radar electromagnetic waves scattered by the object to be detected. Design parameters and characteristics of remote sensing systems are carefully discussed in the abundant literature on the subject, mainly in terms of frequency, waveforming and the geometry of the radar beam that will best suit the detection purposes generally aiming for a required resolution and depth of the analysis on the ground. Good examples can be found in [6]–[11]. However, there are few studies that characterize the variability that the geometry and composition of the underground object, the landmine, introduces in the detection system. This article uses available data on the electromagnetic characterization of plastic mines and soils together with electromagnetic simulations using finite boundary element techniques to analyze the variability of the response to radar waves in the particular case of plastic anti-personnel and anti-tank landmines in order to show the relevance of particular responses of different targets in the design of a GPR system and the importance of estimating and predicting these effects.

II. The Scenario for Landmine Detection

For this study two plastic landmines have been chosen: the PRB-M35 anti-personnel mine and the PRB-M3 anti-tank mine. Both landmines are Belgian and were built until they were banned by Belgium's legislation in March 1995. These landmines are placed in many spots around the world, most of them on desertic grounds; for example: Angola, Chad, Eritrea, Etiopy, Iraq, Jordan, Lebanon, Peru, Somalia, Sudan [3] and Chile [12].

A landmine buried in the ground has a distinct combination of electrical conductivity, electric permittivity, magnetic permeability, and geometrical shape and size. When a landmine is exposed to an electromagnetic wavefront produced by a GPR system above the ground, the scattered reflections caused will depend on these characteristics in comparison to those of the surrounding soil. The characteristics of the incident wavefront, mainly the direction of propagation and the frequency, will also determine the quality of the reflected electromagnetic wavefront. The reflection produced by the buried object is used by remote sensing techniques to produce the detection. When the buried object is metallic it largely reflects any

Fig. 1. Photograph of a PRB-M35 anti-personnel landmine as seen in *Jane's Mines and Mine Clearance* [3].

Fig. 2. Photograph of a PRB-M3 anti-vehicle landmine as seen in *Jane's Mines and Mine Clearance* [3].

incoming electromagnetic wavefront due to the reflectivity of high electrical conducting metals. For this reason many modern mines, Minimum Metal Mines, use plastic cases and contain as little metal as 1 gram (used for critical parts of the detonator), drastically reducing the mine's reflectivity and thus greatly limiting the detection performance of remote sensing techniques. The chosen landmines present classical size and geometry characteristics among the gamut of landmines deployed. The PRB-M35 anti-personnel landmine consist in a small cylindrical body of 65mm diameter with a smaller cylindrical firing device on top, with a total of 60mm height. The PRB-M3 anti-vehicle landmine has a much larger boxed shaped body of 230mm wide also with a smaller cylindrical body on the top, for a total of 130mm height. Figure 1 and Figure 2 show photographs of the PRB-M35 and PRB-M3 landmines. The soil considered for this study are the desertic ones found in the North of Chile, one of the driest on Earth, for which experimental data on the its electromagnetic characteristics exists.

Available experimental data indicates that the plastic in landmines and the desert soils can be accurately represented by non-magnetic, non-conducting dielectrics. The scenario for the analysis of the electromagnetic response of an underground mine can thus be modeled by a dielectric bounded domain with a given relative electric permittivity ε_i (representing the landmine) surrounded by a second dielectric domain with a given relative electric permittivity ε_e (representing the soil). Acceptable values for these permittivities lay near $\varepsilon_i = 2.9$ for the Chilean desertic soil [12], [13] and $\varepsilon_e = 2.5$ for the chosen landmines [14]. These values are also in accordance to broader measurements performed on a wider gamut of soils worldwide [15], [16]. The electromagnetic response is further analyzed with the use of BEM methods to solve the integral representation of the governing Maxwell equations as derived by Ylä-Oijala et al. in [17] using the semi-analytical integration and the direction-dependant expression of the scattered fields derived by A. Bendali and C. Devys in [18].

III. BEM Method for the Integral Representation

Let Ω_i (of relative electric permittivity ε_i) and Ω_e (of relative electric permittivity ε_e) denote the interior and the exterior domain of the mine respectively, and let Γ denote the boundary surface. Let $\mathbf{E}_i = \mathbf{E}_i^a + \mathbf{E}_i^s$ and $\mathbf{H}_i = \mathbf{H}_i^a + \mathbf{H}_i^s$ be the electric and magnetic fields respectively in Ω_i, and let $\mathbf{E}_e = \mathbf{E}_e^a + \mathbf{E}_e^s$ and $\mathbf{H}_e = \mathbf{H}_e^a + \mathbf{H}_e^s$ be electric and magnetic field in Ω_e, where $\mathbf{E}_e^a$ and $\mathbf{H}_e^a$ are the applied incident fields and $\mathbf{E}_e^s$ and $\mathbf{H}_e^s$ are the fields scattered by the object Ω_i representing the landmine. No fields are applied inside Ω_i, $\mathbf{E}_i^a = \mathbf{H}_i^a = \mathbf{0}$, thus leaving $\mathbf{E}_i = \mathbf{E}_i^s$ and $\mathbf{H}_i = \mathbf{H}_i^s$. We define the electric and magnetic current densities over the inner face of Γ as

$$\mathbf{j}_i = -\hat{\mathbf{n}} \times \mathbf{H}_i^s \text{ and } \mathbf{m}_i = \hat{\mathbf{n}} \times \mathbf{E}_i^s, \tag{1}$$

and the electric and magnetic current densities over the external face of Γ as

$$\mathbf{j}_e = \hat{\mathbf{n}} \times \mathbf{H}_e \text{ and } \mathbf{m}_i = -\hat{\mathbf{n}} \times \mathbf{E}_e, \tag{2}$$

respectively, where $\hat{\mathbf{n}}$ is the unit normal of Γ pointing into Ω_e.

The conditions on the boundary of the two dielectric media, Ω_i and Ω_e, enforce the continuity of the tangential fields across Γ, thus imposing

$$\mathbf{j}_e = -\mathbf{j}_i \text{ and } \mathbf{m}_e = \mathbf{m}_i. \tag{3}$$

The scattered electromagnetic fields in Ω_i or in Ω_e can be expressed as a function of the electric and magnetic currents as

$$\mathbf{E}_n^s(\mathbf{x}) = -\frac{1}{\mathrm{i}\omega\varepsilon_0\varepsilon_n}\Phi_n(\mathbf{j}_n, \mathbf{x}) - \Psi_n(\mathbf{m}_n, \mathbf{x}), \tag{4}$$

and

$$\mathbf{H}_n^s(\mathbf{x}) = -\frac{1}{\mathrm{i}\omega\mu_0}\Phi_n(\mathbf{m}_n, \mathbf{x}) + \Psi_n(\mathbf{j}_n, \mathbf{x}), \tag{5}$$

with $n \in \{i, e\}$ indicating the interior or exterior domain.

The integral operators Φ_n and Ψ_n for a given field $\mathbf{f} : \Gamma \to I\!R^3$ are defined as

$$\begin{aligned}\Phi_n(\mathbf{f}, \mathbf{x}) =& \nabla \int_\Gamma G_n(\mathbf{x}, \mathbf{y}) \nabla_\Gamma \cdot \mathbf{f}(\mathbf{y}) \, d\Gamma(\mathbf{y}) \\ &+ \omega^2 \varepsilon_n \varepsilon_0 \mu_0 \int_\Gamma G_n(\mathbf{x}, \mathbf{y}) \mathbf{f}(\mathbf{y}) \, d\Gamma(\mathbf{y}),\end{aligned} \tag{6}$$

and

$$\Psi_n(\mathbf{f}, \mathbf{x}) = \int_\Gamma \nabla G_n(\mathbf{x}, \mathbf{y}) \times \mathbf{f}(\mathbf{y}) \, d\Gamma(\mathbf{y}), \tag{7}$$

where ∇_Γ is the surface divergence of a vector field tangential to Γ, ε_0 and μ_0 are the vacuum's electric permittivity and magnetic permeability, $\omega = 2\pi f$ is the pulsation, and

$$G_n(\mathbf{x}, \mathbf{y}) = \frac{e^{\mathrm{i}\omega\sqrt{\varepsilon_n\varepsilon_0\mu_0}|\mathbf{x}-\mathbf{y}|}}{4\pi|\mathbf{x}-\mathbf{y}|}, \tag{8}$$

is the space Green's function in the interior or the exterior domain.

Using the integral representations in (4) and (5) the EFIE can be written for each domain as

$$\left(\frac{\Phi_n\left(\mathbf{j}_n,\mathbf{x}\right)}{\mathrm{i}\omega\varepsilon_0\varepsilon_n}+\Psi_n\left(\mathbf{m}_n,\mathbf{x}\right)+\frac{1}{2}\hat{\mathbf{n}}\times\mathbf{m}_n\right) = -\hat{\mathbf{n}}\times\left(\hat{\mathbf{n}}\times\mathbf{E}_n^a\right). \tag{9}$$

The surface Γ is discretized in a triangular mesh Γ_d with M edges and to each edge a Rao-Wilton-Glisson (RWG) function is associated producing the set of RWG bases $\{\mathbf{f}_m\}_{m=1}^M$. Approximations to the external electrical and magnetic surface currents can be represented in Γ_d as

$$\mathbf{j}_e^d=\sum_{m=1}^M\alpha_m\mathbf{f}_m,\text{ and }\mathbf{m}_e^d=\sum_{m=1}^M\beta_m\mathbf{f}_m, \tag{10}$$

and the inner currents as

$$\mathbf{j}_i^d=-\sum_{m=1}^M\alpha_m\mathbf{f}_m,\text{ and }\mathbf{m}_i^d=-\sum_{m=1}^M\beta_m\mathbf{f}_m. \tag{11}$$

The variational formulation for the EFIE (9) in Ω_i and Ω_e is then discretized using the approximated currents and it is transformed in a linear system for the $2M$ unknowns $\{\alpha_m\}_{m=1}^M$ and $\{\beta_m\}_{m=1}^M$ using the Galerkin method.

$$\begin{bmatrix}\mathbf{Z}^{J,e} & \mathbf{Z}^{M,e}\\ \mathbf{Z}^{J,i} & \mathbf{Z}^{M,i}\end{bmatrix}\begin{bmatrix}\mathbf{I}^J\\ \mathbf{I}^M\end{bmatrix}=\begin{bmatrix}\mathbf{V}^e\\ \mathbf{0}\end{bmatrix} \tag{12}$$

In the linear system (12) the vectors $\mathbf{I}^J$ contain $\mathbf{I}^M$ the unknowns representing the electric currents ($\{\alpha_m\}_{m=1}^M$) and the unknown representing the magnetic currents ($\{\beta_m\}_{m=1}^M$) respectively. The elements of the impedance submatrixes are:

$$Z_{n.m}^{J,e}=\frac{1}{\mathrm{i}\omega\varepsilon_0\varepsilon_e}\int_{\Gamma_d}\nabla\cdot\mathbf{f}_m(\mathbf{x})\int_{\Gamma_d}G_e(\mathbf{x},\mathbf{y})\nabla_\Gamma\cdot\mathbf{f}_n(\mathbf{y})dS(\mathbf{y})dS(\mathbf{x}) +\mathrm{i}\omega\mu_0\int_{\Gamma_d}\mathbf{f}_m(\mathbf{x})\cdot\int_{\Gamma_d}G_e(\mathbf{x},\mathbf{y})\mathbf{f}_n(\mathbf{y})dS(\mathbf{y})dS(\mathbf{x}), \tag{13}$$

$$Z_{n.m}^{M,e}=\int_{\Gamma_d}\mathbf{f}_m(x)\cdot\int_{\Gamma_d}\nabla G_e(\mathbf{x},\mathbf{y})\times\mathbf{f}_n(\mathbf{y})dS(\mathbf{y})dS(\mathbf{x}) -\frac{1}{2}\int_{\Gamma_d}\mathbf{f}_m(\mathbf{x})\cdot(\hat{\mathbf{n}}\times\mathbf{f}_n(\mathbf{x}))dS(\mathbf{x}), \tag{14}$$

$$Z_{n.m}^{J,i}=\frac{1}{\mathrm{i}\omega\varepsilon_0\varepsilon_i}\int_{\Gamma_d}\nabla\cdot\mathbf{f}_m(\mathbf{x})\int_{\Gamma_d}G_i(\mathbf{x},\mathbf{y})\nabla_\Gamma\cdot\mathbf{f}_n(\mathbf{y})dS(\mathbf{y})dS(\mathbf{x}) +\mathrm{i}\omega\mu_0\int_{\Gamma_d}\mathbf{f}_m(\mathbf{x})\cdot\int_{\Gamma_d}G_i(\mathbf{x},\mathbf{y})\mathbf{f}_n(\mathbf{y})dS(\mathbf{y})dS(\mathbf{x}), \tag{15}$$

$$Z_{n.m}^{M,i}=\int_{\Gamma_d}\mathbf{f}_m(x)\cdot\int_{\Gamma_d}\nabla G_i(\mathbf{x},\mathbf{y})\times\mathbf{f}_n(\mathbf{y})dS(\mathbf{y})dS(\mathbf{x}) +\frac{1}{2}\int_{\Gamma_d}\mathbf{f}_m(\mathbf{x})\cdot(\hat{\mathbf{n}}\times\mathbf{f}_n(\mathbf{x}))dS(\mathbf{x}). \tag{16}$$

And the excitation vector $\mathbf{V}^e$ is

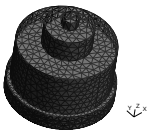

Fig. 3. Mesh representation of a PRB-M35 anti-personnel landmine, composed by 2068 triangular faces and 3102 edges (longest edge, 7mm).

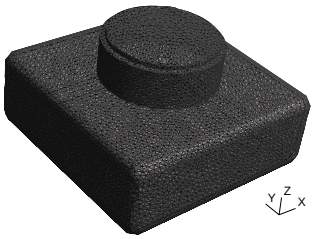

Fig. 4. Mesh representation of a PRB-M3 anti-vehicle landmine, composed by 5356 triangular faces and 8034 edges (longest edge, 17mm).

$$V_m^e=-\int_{\Gamma_d}\mathbf{f}_m(\mathbf{x})\cdot\mathbf{E}_e^a(\mathbf{x})dS(\mathbf{x}). \tag{17}$$

Discretizing the geometries of the selected landmines in triangular meshes allows for the computation of their scattered fields when in the presence of incident wavefront applied using a GPR system.

IV. Frequency Response and Scattering Pattern

Once the electric and magnetic currents have been obtained by solving the linear system (12) the scattered electric field $\mathbf{E}_e^s$ in Ω_e can be computed using the integral representation (4) now supported in the discretized surface Γ_d. If the point of calculation $\mathbf{x}\in\Omega_e$ of the electric field $\mathbf{E}_e^s$ is written separating the range and direction component as $\mathbf{x}=r\hat{\mathbf{u}}$, where r account for the distance to the point and $\hat{\mathbf{u}}$ for its direction, the electric field can be written separating the range-dependant and direction-dependant components for a given pulsation ω as

$$\mathbf{E}_e^s(\omega,r,\hat{\mathbf{u}})=\frac{\mathrm{i}\omega\mu_0}{4\pi}\frac{e^{\mathrm{i}\omega\sqrt{\varepsilon_0\mu_0}r}}{r}(\mathbf{P}(\omega,\hat{\mathbf{u}})-(\mathbf{P}(\omega,\hat{\mathbf{u}})\cdot\hat{\mathbf{u}})\hat{\mathbf{u}} +\mathbf{Q}(\omega,\hat{\mathbf{u}})\times\hat{\mathbf{u}}), \tag{18}$$

where $\mathbf{P}(\omega,\hat{\mathbf{u}})$ and $\mathbf{Q}(\omega,\hat{\mathbf{u}})$ are given by the following expressions:

$$\mathbf{P}(\omega,\hat{\mathbf{u}})=\int_{\Gamma_d}e^{\mathrm{i}\omega\sqrt{\varepsilon_e\varepsilon_0\mu_0}\mathbf{y}\cdot\hat{\mathbf{u}}}\mathbf{j}_e^d(\mathbf{y})d\Gamma_d(\mathbf{y}), \tag{19}$$

$$\mathbf{Q}(\omega,\hat{\mathbf{u}})=\frac{1}{\mathrm{i}\omega\mu_0}\int_{\Gamma_d}e^{\mathrm{i}\omega\sqrt{\varepsilon_e\varepsilon_0\mu_0}\mathbf{y}\cdot\hat{\mathbf{u}}}\mathbf{m}_e^d(\mathbf{y})d\Gamma_d(\mathbf{y}). \tag{20}$$

The radar cross-section seen from a given direction $\hat{\mathbf{u}}$, while illuminated with a harmonic radar wavefront of pulsation ω can thus be written as

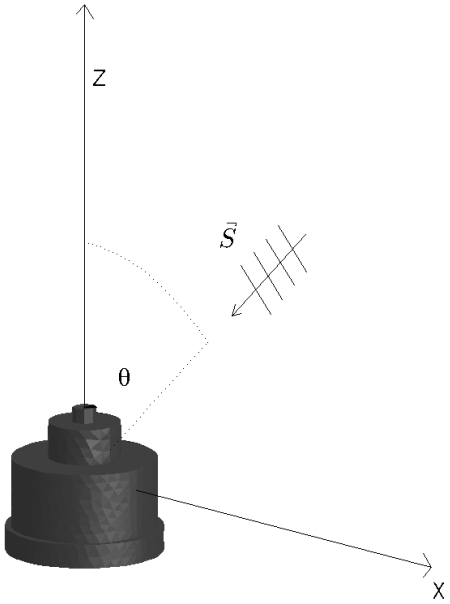

Fig. 5. Angle convention for the incident and diffracted field. The incident wavefront of fixed frequency comes from a direction contained in the XZ plane and given by the angle θ measured from the vertical direction Z.

$$\sigma(\omega,\hat{\mathbf{u}}) = \frac{\omega^2\mu_0^2}{4\pi}|\mathbf{P}(\omega,\hat{\mathbf{u}}) - (\mathbf{P}(\omega,\hat{\mathbf{u}})\cdot\hat{\mathbf{u}})\hat{\mathbf{u}} + \mathbf{Q}(\omega,\hat{\mathbf{u}})\times\hat{\mathbf{u}}|^2. \quad (21)$$

The radar cross-section is used as an indicator of detectability of a landmine under a GPR system using a given incident field, with a given frequency, and given incident and observed directions. Illuminating a landmine from a given frequency $\omega = 2\pi f$ and direction of incidence ($\vec{S}$), measured as θ from the vertical direction (Z axis, $\theta = 0°$), and registering the RCS as seen from different directions within a plane (XZ plane, $\hat{\mathbf{u}} = (sin(\phi), 0, cos(\phi))^T$, with $\phi \in [0, 360°]$) containing the direction of incidence and the vertical direction, the detectability can be studied for different frequencies, and different directions for illumination and observation. In all the simulations presented in the results the wavefront is polarized such that the electric field is normal to the XZ plane. Figure 5 shows a landmine with the spatial elements described and used to express the results of the simulations conducted with the methodology described in Section III.

Figures 6 and 7 show the RCS in square meters (m^2) for a range of frequencies, for the PRB-M35 and PRB-M3 respectively, when the incident electromagnetic front comes downwards from the vertical direction ($\theta = 0°$) and the response is measured for and observer also above the mine in the vertical direction ($\hat{\mathbf{u}} = (0, 0, 1)^T$). Different soils have been used (with electric permittivities ε_e of 1.7, 2.1 and 2.9) and the electric permittivity of the plastic landmine ε_i has been set to 2.5, as stated in Section II.

The next figures show the angular dispersion of the scattered wavefront on the directions comprised on the XZ plane ($\hat{\mathbf{u}} = (sin(\phi), 0, cos(\phi))^T, \phi \in [0, 360°]$) when the landmine is illuminated from a given direction measured by an angle

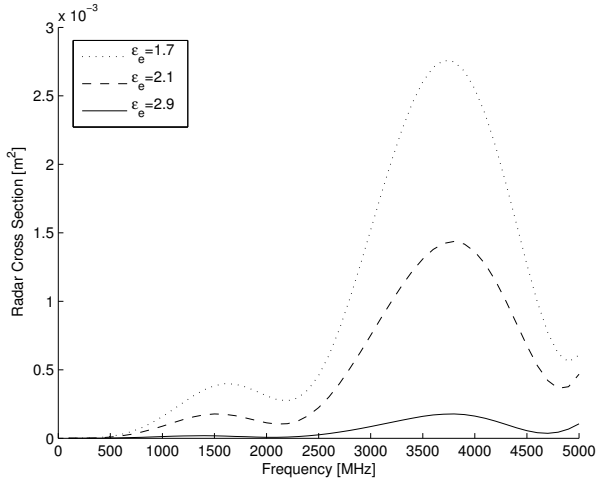

Fig. 6. RCS of the PRB-M35 anti-personnel landmine measured in square meters (m^2) for a for a range of frequencies when viewed illuminated and observed from above ($\theta = 0°$, $\hat{\mathbf{u}} = (0, 0, 1)^T$).

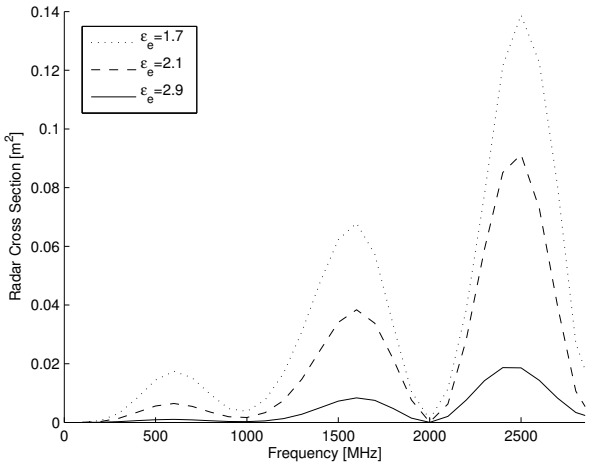

Fig. 7. RCS of the PRB-M3 anti-personnel landmine measured in square meters (m^2) for a for a range of frequencies when viewed illuminated and observed from above ($\theta = 0°$, $\hat{\mathbf{u}} = (0, 0, 1)^T$).

θ from the vertical direction Z indicated in each figure, and the incident wavefront has a fixed frequency f. Figures 8, 9 and 10 show the angular dispersion of the incident wavefront scattered by a PRB-M35 anti-personnel landmine when illuminated from different directions ($\theta = 0°$, $\theta = 30°$ and $\theta = 60°$ respectively) at 3.75GHz (a favorable frequency for the detection of this landmine as revealed in figure 6). The electric permittivity of the soil ε_e has been set to 2.9 and the electric permittivity of the landmine ε_i has been set to 2.5 in accordance with the data discussed in Section II.

Figures 11, 12 and 13 show the angular dispersion of the incident wavefront scattered by a PRB-M3 anti-vehicle landmine when illuminated from different directions ($\theta = 0°$, $\theta = 30°$ and $\theta = 60°$ respectively) at 2.4GHz (a favorable frequency for the detection of this landmine as revealed in figure 7).

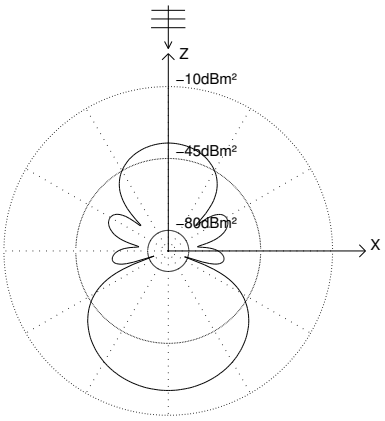

Fig. 8. RCS of the PRB-M35 anti-personnel mine in decibels of square meters (dBm^2) observed in directions contained in the XZ plane ($\hat{\mathbf{u}} = (sin(\phi), 0, cos(\phi))^T, \phi \in [0, 360°]$) when an incident wavefront at 3.75GHz comes from $\theta = 0°$.

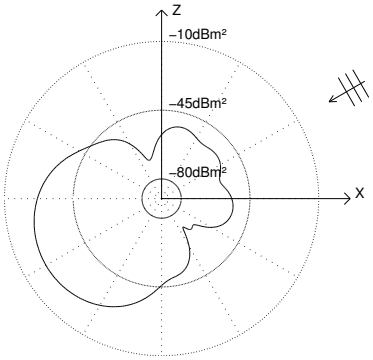

Fig. 10. RCS of the PRB-M35 anti-personnel mine in decibels of square meters (dBm^2) observed in directions contained in the XZ plane ($\hat{\mathbf{u}} = (sin(\phi), 0, cos(\phi))^T, \phi \in [0, 360°]$) when an incident wavefront at 3.75GHz comes from $\theta = 60°$.

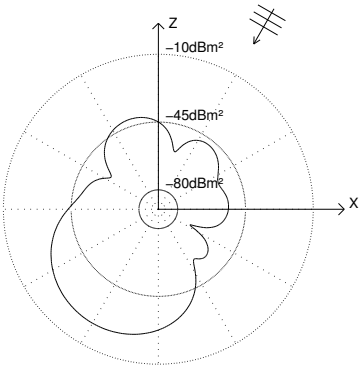

Fig. 9. RCS of the PRB-M35 anti-personnel mine in decibels of square meters (dBm^2) observed in directions contained in the XZ plane ($\hat{\mathbf{u}} = (sin(\phi), 0, cos(\phi))^T, \phi \in [0, 360°]$) when an incident wavefront at 3.75GHz comes from $\theta = 30°$.

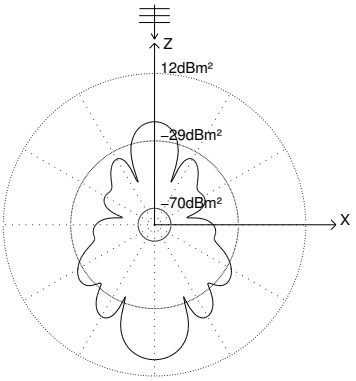

Fig. 11. RCS of the PRB-M3 anti-vehicle mine in decibels of square meters (dBm^2) observed in directions contained in the XZ plane ($\hat{\mathbf{u}} = (sin(\phi), 0, cos(\phi))^T, \phi \in [0, 360°]$) when an incident wavefront at 2.4GHz comes from $\theta = 0°$.

V. Conclusion

The results of the simulations show the different electromagnetic response, the detectability measured as RCS, for two different landmines, different materials and more importantly for different incident radar wavefront with different frequencies and angles of incidence. It follows from these results that two different landmines as the ones used in this research, which can be present in the same minefields as it is the care in Chile, can present different degrees of detectability for a single GPR system. These differences can impose difficulties for the design of detection systems as the RCS one mine can be tens of times higher than others also present in the same field. Also, for each landmine different frequencies can induce minimal responses, registering a RCS fading for particular wavelengths in the scanning frequency of a GPR system. In the case studied a system operating at 2.4GHz could maximize the probability of detection of the PRB-M3 landmine within a normal GPR frequency range (Figure 7) but sacrificing detection capabilities for the PRB-M35 landmine (Figure 6). In a similar way, different incidence angles at difference frequencies will affect different mine differently, as shown in Figures 8, 9, 10, 11, 12 and 13, where deep RCS fading can occur in angles normally considerer in the design of GPR systems. Thus, the specific responses of the landmines known to be present at a given minefield must be simulated, predicted, and taken into account when designing GPR detection systems.

Acknowledgment

Pedro Ramaciotti is supported by the collaboration of the program MECE Educación Superior (2) of the Pontificia Universidad Católica.

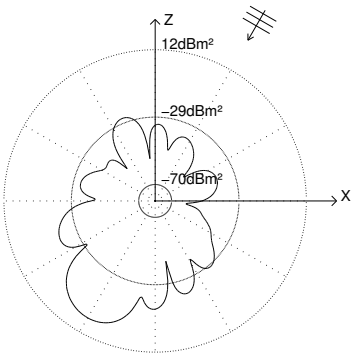

Fig. 12. RCS of the PRB-M3 anti-vehicle mine in decibels of square meters (dBm^2) observed in directions contained in the XZ plane ($\hat{\mathbf{u}} = (sin(\phi), 0, cos(\phi))^T, \phi \in [0, 360°]$) when an incident wavefront at 2.4GHz comes from $\theta = 30°$.

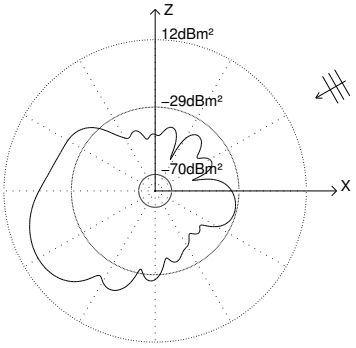

Fig. 13. RCS of the PRB-M3 anti-vehicle mine in decibels of square meters (dBm^2) observed in directions contained in the XZ plane ($\hat{\mathbf{u}} = (sin(\phi), 0, cos(\phi))^T, \phi \in [0, 360°]$) when an incident wavefront at 2.4GHz comes from $\theta = 60°$.

The authors would also like to thank the collaboration of the Academia Politécnica Militar (ACAPOMIL) of the Chilean Army for its constant support in providing relevant information, technical data and context when required in the advance of demining initiatives and particularly in this research.

REFERENCES

[1] *Landmine Monitor 2010*. International Campaing to Ban Landmines, 2010.

[2] *Annual Report 2009*. GICHD, Geneve International Centre for Humanitarian Demining, 2009.

[3] C. King, *Jane's Mines and Mine Clearance*, 4th ed., 1999-2000.

[4] D. Daniels, D. Gunton, and H. Scott, "Introduction to subsurface radar," *Radar and Signal Processing, IEE Proceedings F*, vol. 135, no. 4, pp. 278–320, 1988.

[5] D. J. Daniels, "A review of landmine detection using gpr," *Technology*, pp. 280–283, October 2008.

[6] M. Bhuiyan and B. Nath, "Anti-personnel mine detection and classification using gpr image," *18th International Conference on Pattern Recognition*, 2006.

[7] Z. You, J. Cross, K. Foo, P. Atkins, A. Thomas, G. Curioni, and A. Islas-Cital, "Disposable stepped-frequency gpr and soil measurement devices," *13th International Conference on Ground Penetrating Radar (GPR)*, June 2010.

[8] L. D. Donato, I. Catapano, F. Soldovieri, and L. Crocco, "Imaging of 3d magnetic targets from multiview multistatic gpr data," *13th International Conference on Ground Penetrating Radar (GPR)*, 2010.

[9] T. Savelyev, L. van Kempen, H. Sahli, J. Sachs, and M. Sato, "Investigation of time–frequency features for gpr landmine discrimination," *IEEE Transactions on Geoscience and Remote Sensing*, vol. 45, no. 1, pp. 118–129, Jan 2007.

[10] U. Uschkerat, "Performance evaluation of a gpr system for mine detection using a 3d-sar algorithm," *2010 11th International Radar Symposium*, pp. 1–3, 2010.

[11] U. Oguz and L. Gurel, "Three-dimensional fdtd modeling of a gpr," *IEEE Antennas and Propagation Society International Symposium*, vol. 4, pp. 1990–1993, 2000.

[12] *Detection of Landmines in the North of Chile by means of Ground Penetrating Radar*, Columbus, Ohio, June 2006.

[13] *Airborne GPR measurements in the Atacama Desert - first results and constraints using a 150MHz pulse radar for groundwater exploration*, Columbus, Ohio, June 2006.

[14] B. Riddle, J. Baker-Jarvis, and J. Krupka, "Complex permittivity measurements of common plastics over variable temperatures," *IEEE Transactions on Microwave Theory and Techniques*, vol. 51, no. 3, pp. 727–733, March 2003.

[15] T. W. Miller, B. Borchers, J. M. H. Hendrickx, S.-H. Hong, L. W. Dekker, and C. J. Ritsema, "Effects of soil physical properties on gpr for landmine detection," *Bosque*, pp. 1–10, 2002.

[16] G. Cross and D. Benson, *Soil Properties and GPR Detection of Landmines: A Basis for Forecasting and Evaluation of GPR Performance*, 1999.

[17] P. Ylä-Oijala, M. Taskinen, and J. Sarvas, "Surface integral equation method for general composite metallic and dielectric structures with junctions," *Progress In Electromagnetics Research*, vol. 52, pp. 81–108, 2005.

[18] C. D. A. Bendali, "Calcul numérique du rayonnement de cornets électromagnétiques dont l'ouverture est partiellement remplie par un diélectrique," *Onde électrique*, vol. 66, no. 1, pp. 77–81, 1986.